Nanoscale

REVIEW

View Article Online
View Journal | View Issue



Cite this: *Nanoscale*, 2026, **18**, 1179

# Modeling the stability diagram and electrical conductance of a tunneling resonance system based on a carbon nanotube quantum dot

Ali Moulhim*[a] and Ali A. Khairbek *[b]

Received 29th July 2025,
Accepted 13th November 2025

DOI: 10.1039/d5nr03208c

rsc.li/nanoscale

Carbon nanotubes (CNTs) and CNT-based quantum dots (CNTQDs) hold significant promise for next-generation quantum and digital computing devices. This study presents a comprehensive theoretical analysis of the electronic properties of CNTs and CNTQDs, focusing on their stability diagrams and electrical conductance characteristics. Using the constant interaction model (CIM) and Green's function formalism within the Keldysh framework, we derive the quantized energy levels of the CNTQDs, evaluate their Coulomb blockade phenomena, and deduce the electrical conductance through the CNTQDs. This study illustrates how valley and spin degeneracy lead to the creation of four blockade diamonds as well as four conductance peaks per quantized energy level. The stability diagrams help in designing stable transistors and qubits that exhibit a voltage map that can be used for control in these devices.



## 1. Introduction

While electronics industries have reached close to the end of the silicon age, scientists have been investigating suitable materials or new devices with higher computational powers that can replace silicon-based transistors in the last three decades. Researchers are pursuing two parallel paths: designing compact, high-efficiency transistors for digital computing using new materials and exploring quantum computing techniques with suitable materials that leverage quantum states, such as qubits, for advanced computation.[1–11] Carbon nanotubes have emerged as key dual-use materials, enabling the fabrication of digital devices such as new field transistors for digital computing and spin qubits, valley qubits, and charge qubits for quantum systems.[12–25]

The exceptional properties of carbon nanotubes have attracted researchers to investigate useful applications for high-efficiency computational devices. The electronic properties of CNTs have been studied since they were discovered.[26,27] The transport properties, such as confining phenomena and the Coulomb blockade effect for electrons as well as ions,[28–32] valley degeneracy,[33,34] spintronics effects,[35,36] Fabry–Pérot interference of confined electrons,[37,38] and single-electron transport phenomena,[39,40] have been reported. CNTs exhibit induced superconductivity under many conditions, such as small-diameter CNTs,[41,42] doping with boron and nitrogen,[43,44] topological superconductivity under curvature effects,[45,46] and interfacing between CNTs and superconducting materials.[47] CNTs have been shown to be a high-efficiency resource for single-photon diodes and to enhance the efficiency of light absorption for better-performing photovoltaic devices.[48–51] Carbon nanotube quantum dots (CNTQDs) have attracted significant attention for quantum computing applications due to their ability to host spin, valley, and charge qubits.[16–25] Recently, qubits based on CNTs have been used in quantum communication experiments.[52,53] Using CNTs to design a device for a desired application and better efficiency requires an understanding of the electronic structures and how electrons can be transported in (to) them.

This paper shows how the energy dispersion relationships of different types of CNTs can be calculated, illustrating how CNTs can be electrically classified on the basis of chiral indices. The quantized energy levels and the additional charge energy at every sublevel of the CNTQDs are discussed. The confinement phenomenon of the CNTQDs was analyzed *via* a constant interaction model (CIM), and the electrical conductance was analyzed *via* quantum field theory to determine their stability. This would help in designing CNTQDs for various applications.

## 2. Graphene and carbon nanotube QDs

### 2.1. Graphene and carbon nanotube structure

A carbon nanotube is derived from graphene, a two-dimensional material of carbon atoms arranged in a hexagonal struc-

[a]*School of Physics, Beijing Institute of Technology, Beijing 100081, China. E-mail: alimoulhim@gmail.com, 3820232060@bit.edu.cn*
[b]*Department of Chemistry, Faculty of Science, Latakia University, Latakia, Syrian Arab Republic. E-mail: alikhairbek@gmail.com*

ture. The unit cell of graphene has a triangular shape and consists of two carbon atoms (see Fig. 1 (a)). The two basis vectors of the graphene unit cell are:[26,27]

$$\boldsymbol{a_1} = a_0\frac{3}{2}\boldsymbol{i} + a_0\frac{\sqrt{3}}{2}\boldsymbol{j} = a_0\left(\frac{3}{2},\frac{\sqrt{3}}{2}\right)$$
$$\boldsymbol{a_2} = a_0\frac{3}{2}\boldsymbol{i} - a_0\frac{\sqrt{3}}{2}\boldsymbol{j} = a_0\left(\frac{3}{2},-\frac{\sqrt{3}}{2}\right) \quad (1)$$

where $a_0 \approx 1.42$ Å is the carbon–carbon distance. The reciprocal lattice vectors of graphene $\boldsymbol{b_1}$ & $\boldsymbol{b_2}$ can be defined by using $\boldsymbol{a_i b_j} = 2\pi\delta_{ij}$ $(i, j = 1, 2)$ and are given by:

$$\boldsymbol{b_1} = \frac{4\pi}{3a_0}\left(\frac{1}{2},\frac{\sqrt{3}}{2}\right) \qquad \boldsymbol{b_2} = \frac{4\pi}{3a_0}\left(\frac{1}{2},-\frac{\sqrt{3}}{2}\right) \quad (2)$$

As illustrated in Fig. 1(b), the first Brillouin zone of graphene can be defined by constructing the perpendicular bisectors of the reciprocal lattice vectors. This first Brillouin zone has a hexagonal shape, with the corners defined as Dirac points. The positions of the Dirac points ($\boldsymbol{K}$ and $\boldsymbol{K'}$) in reciprocal lattice space (momentum space) are as follows:

$$\boldsymbol{K}, \boldsymbol{K'} = \frac{2\pi}{3a_0}\left(\mp 1,\frac{1}{\sqrt{3}}\right), \quad \frac{2\pi}{3a_0}\left(\mp 1,-\frac{1}{\sqrt{3}}\right), \quad \frac{2\pi}{3a_0}\left(\mp\frac{2}{\sqrt{3}},0\right) \quad (3)$$

The dispersion relation of bulk graphene is given by:[54,55]

$$\varepsilon_i^{\pm}(k) = \pm t\sqrt{1 + 4\cos\left[\frac{3}{2}k_x a_0\right]\cos\left[\frac{\sqrt{3}}{2}k_y a_0\right] + 4\cos^2\left[\frac{\sqrt{3}}{2}k_y a_0\right]} \quad (4)$$

where $t \approx 2.7$ eV is the nearest-neighbor hopping term of graphene. In this context, the (+) symbol represents the conduction band, whereas the (−) symbol corresponds to the valence band. These bands meet at the Dirac points. As a result, graphene is considered a zero-bandgap semiconductor. Near the Dirac points, the dispersion relation can be approximated by a linear equation:[45]

$$\varepsilon_i^{\pm} = \pm\hbar v_F\sqrt{{\kappa_x}^2 + {\kappa_y}^2}; \quad v_F = \frac{3}{2\hbar}ta_0 \quad (5)$$

where $v_F = \frac{3}{2\hbar}ta_0$. A carbon nanotube (CNT) is formed by rolling a graphene sheet into a concentric cylindrical shape (Fig. 1(c)). The structural characteristics of CNTs, which play crucial roles in determining their electronic properties, could be derived from the geometric structure of graphene. The circumference of the CNT is defined by the *chiral vector*, which is expressed in terms of the basis vectors of graphene as follows:

$$\boldsymbol{C_h} = n\boldsymbol{a_1} + m\boldsymbol{a_2} \quad (6)$$

Here, $(n,m)$ are known as the chiral indices. The circumference of a carbon nanotube is given by $|\boldsymbol{C_h}| = \sqrt{3}a_0\sqrt{n^2 + m^2 + nm} = \pi d$, where $d$ is the diameter of the nanotube. The chiral vector $\boldsymbol{C_h}$ defines the first vector of the nanotube's unit cell. The shortest vector perpendicular to $\boldsymbol{C_h}$ and parallel to the tube axis is called the translational vector $\boldsymbol{T}$. This vector represents the second vector of the nanotube unit cell. Mathematically, it is expressed in terms of the graphene basis vectors of $\boldsymbol{a_1}$ and $\boldsymbol{a_2}$ as follows:

$$\boldsymbol{T} = \frac{2m+n}{N_R}\boldsymbol{a_1} - \frac{2n+m}{N_R}\boldsymbol{a_2} = \frac{3}{2}a_0\frac{m-n}{N_R}\boldsymbol{i} + \frac{3\sqrt{3}}{2}a_0\frac{(m+n)}{N_R}\boldsymbol{j}. \quad (7)$$

where $N_R = \gcd(2m + n, 2n + m)$ is the greatest common divisor of $2m + n$ and $2n + m$, which is obtained from the condition $\boldsymbol{C_h}\cdot\boldsymbol{T} = 0$. The length of the translational vector is:[26,27]

$$\boldsymbol{T} = \frac{\sqrt{3}a_0\sqrt{n^2 + m^2 + nm}}{N_R} = \frac{\sqrt{3}|\boldsymbol{C_h}|}{N_R}. \quad (8)$$

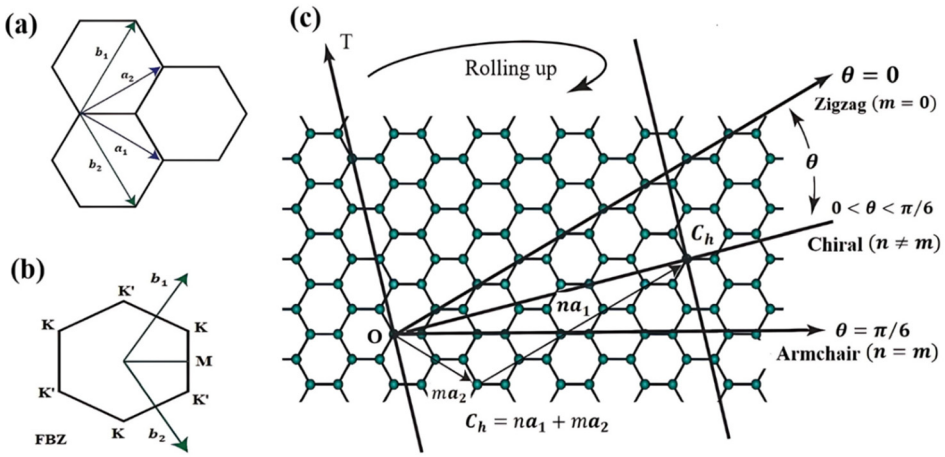


**Fig. 1** (a) Hexagonal monolayer graphene and lattice vectors $\boldsymbol{a_1}$ and $\boldsymbol{a_2}$. (b) Graphene Brillouin zone with reciprocal lattice vectors $\boldsymbol{b_1}$ & $\boldsymbol{b_2}$. (c) The graphene sheet and geometrical parameters of the CNTs.

 

The angle between $\boldsymbol{a_1}$ and $\boldsymbol{C_h}$ is defined as the chiral angle and is given by:

$$\theta = \cos^{-1}\left[\frac{\boldsymbol{C_h}\cdot\boldsymbol{a_1}}{|\boldsymbol{C_h}|\cdot|\boldsymbol{a_1}|}\right] = \cos^{-1}\left[\frac{2m+n}{2\sqrt{n^2+m^2+nm}}\right]. \quad (9)$$

This angle is used to categorize the nanotubes into three different types:

- $\theta = \pi/6$ Armchair CNT with $(n = m)$
- $\theta = 0$ Zigzag CNTs with $(n \neq 0, m = 0)$
- $0 < \theta < \pi/6$ Chiral CNTs with $(n \neq m)$

The total number of graphene unit cells (graphene unit cells) per CNT unit cell is as follows:

$$N_C = \frac{|\boldsymbol{C_h}\times T|}{|\boldsymbol{a_1}\times\boldsymbol{a_2}|} = \frac{2(n^2+m^2+nm)}{N_R} = \frac{2L^2}{{a_0}^2 N_R} \quad (10)$$

This means that there are $2N_C$ carbon atoms in the primitive cell of a carbon nanotube. Since the vectors $\boldsymbol{C_h}$ and $\boldsymbol{T}$ define the Bravais lattice of a carbon nanotube, the reciprocal vectors of a nanotube ($\boldsymbol{K_1}$ and $\boldsymbol{K_2}$) can be defined *via* the following relationships.

$$\boldsymbol{C_h}\cdot\boldsymbol{K_1} = 2\pi \;\&\; \boldsymbol{T}\cdot\boldsymbol{K_1} = 0, \quad \boldsymbol{C_h}\cdot\boldsymbol{K_2} = 2\pi \;\&\; \boldsymbol{T}\cdot\boldsymbol{K_2} = 2\pi. \quad (11)$$

This leads to

$$\begin{aligned}\boldsymbol{K_1} &= \frac{\pi}{a_0(n^2+m^2+nm)}\left[(m+n)\boldsymbol{i} + \left(\frac{n-m}{\sqrt{3}}\right)\boldsymbol{j}\right]\\ \boldsymbol{K_2} &= \frac{\pi N_R}{a_0(n^2+m^2+nm)}\left[\left(\frac{m-n}{3}\right)\boldsymbol{i} + \left(\frac{n+m}{\sqrt{3}}\right)\boldsymbol{j}\right]\end{aligned} \quad (12)$$

where $\boldsymbol{K_1}$ and $\boldsymbol{K_2}$ represent the reciprocal vectors of a nanotube along its circumference (tube axis).

### 2.2. Carbon nanotube energy band structure

Since a carbon nanotube has a cylindrical shape, electrons are confined along the tube's circumference, leading to quantized energy levels in two directions. In contrast, the electron energy along the tube's axis depends on its length: it is continuous for an infinitely long nanotube or quantized for a finite-length nanotube. Thus, the wave vector k in the nanotube can be decomposed into circumferential and axial components accordingly.

$$\boldsymbol{k} = k_\perp\boldsymbol{K_1} + k_\parallel\boldsymbol{K_2}. \quad (13)$$

Here, $k_\perp$ represents the circumferential component of the wave vector, which is perpendicular to the tube axis (along the $\boldsymbol{K_1}$ direction), whereas $k_\parallel$ is the axial component, which is aligned with the tube axis (along the $\boldsymbol{K_2}$ direction). Since a nanotube is formed by rolling a graphene sheet, traversing an integer number of chiral vectors $\boldsymbol{C_h}$ leads back to the same point in space. This periodic boundary condition enables the electron wave function to be expressed as $u_j(\boldsymbol{k},\boldsymbol{r}+\boldsymbol{C_h}) = u_j(\boldsymbol{k},\boldsymbol{r})$, which means that $e^{i\boldsymbol{k}\boldsymbol{C_h}} = 1$. This leads to the following allowed values of $\boldsymbol{k}_\perp$:

$$\boldsymbol{k}\boldsymbol{C_h} = \boldsymbol{k}_\perp\boldsymbol{C_h} = \upsilon 2\pi \Rightarrow |\boldsymbol{k}_\perp| = \upsilon\frac{2\pi}{|\boldsymbol{C_h}|} = \upsilon\frac{2}{d} \quad \text{with } \upsilon = 1,\ldots N_C. \quad (14)$$

In the case of an infinite nanotube, the allowed values of another component, the parallel component $k_\parallel$, form a continuous spectrum but remain confined within a specific range $k_\parallel[-\pi/|\boldsymbol{T}|,\pi/|\boldsymbol{T}|]$. The pair $(\boldsymbol{k}_\perp,\boldsymbol{k}_\parallel)$ defines a series of cutting lines that represent the allowed values of the wave vector in the Brillouin zone. The number, length, orientation, and spacing of these lines, the separation between two adjacent lines $(2/d)$, depend on the chiral indices $(n,m)$ of the carbon nanotube. The energy dispersion of a carbon nanotube can be derived from the energy dispersion of graphene by applying appropriate boundary conditions: one around the nanotube's circumference and the other along its axis. The general expression for the energy dispersion of a carbon nanotube is

$$\begin{aligned}\varepsilon^{\pm}(\boldsymbol{k}) &= \varepsilon_i \pm (\upsilon, k_\parallel)\\ &= \pm t\left[1 + 4\cos\left[\upsilon\frac{3\pi}{N_C N_R}(m+n) + k_\parallel\frac{3a_0}{2\sqrt{2N_C N_R}}(n-m)\right]\cos\left[\upsilon\frac{\pi}{N_C N_R}(n-m) + k_\parallel\frac{3a_0}{2\sqrt{2N_C N_R}}(n+m)\right]\right.\\ &\quad \left. + 4\cos^2\left[\upsilon\frac{\pi}{N_C N_R}(n-m) + k_\parallel\frac{3a_0}{2\sqrt{2N_C N_R}}(n+m)\right]\right]^{\frac{1}{2}}\end{aligned} \quad (15)$$

This equation defines $N$ pairs of energy dispersion curves that result from the cross sections of the two-dimensional energy dispersion surface of 2D graphene, where the cross sections are cut from the lines of $\upsilon\boldsymbol{K_1} + k_\parallel(\boldsymbol{K_2}/|\boldsymbol{K_2}|)$, and they represent the allowed values of the wave vector $k_\parallel$. The space between every two successive lines is $\Delta k_\parallel = 2/d$. For a particular armchair nanotube, where $(n = m)$, the expression of the energy dispersion of carbon nanotubes can be simplified to:

$$\varepsilon^{\pm,a}(\upsilon,k_\parallel) = \pm t\sqrt{1 + 4\cos\left[\upsilon\frac{\pi}{n}\right]\cos\left[\frac{\sqrt{3}}{2}a_0k_\parallel\right] + 4\cos^2\left[\frac{\sqrt{3}}{2}a_0k_\parallel\right]}. \quad (16)$$

with $\Delta k_\parallel = 2\pi/3a_0n$ and $\upsilon = 0, 1,\ldots 2n$. In the case of the zigzag nanotube, where $(n \neq 0, m = 0)$, the energy dispersion of the carbon nanotubes can be simplified to:

$$\varepsilon^{\pm,z}(\upsilon,k_\parallel) = \pm t\sqrt{1 + 4\cos\left[\upsilon\frac{3\pi}{2n} - k_\parallel\frac{3a_0}{4}\right]\cos\left[\upsilon\frac{\pi}{2n} + k_\parallel\frac{3a_0}{4}\right] + 4\cos^2\left[\upsilon\frac{\pi}{2n} + k_\parallel\frac{3a_0}{4}\right]} \quad (17)$$

The energy dispersion relationships for various types of carbon nanotubes are plotted as a function of $k_\parallel$ in Fig. 2. This figure illustrates the differences in electronic properties based on nanotube chirality. In armchair nanotubes, the allowed

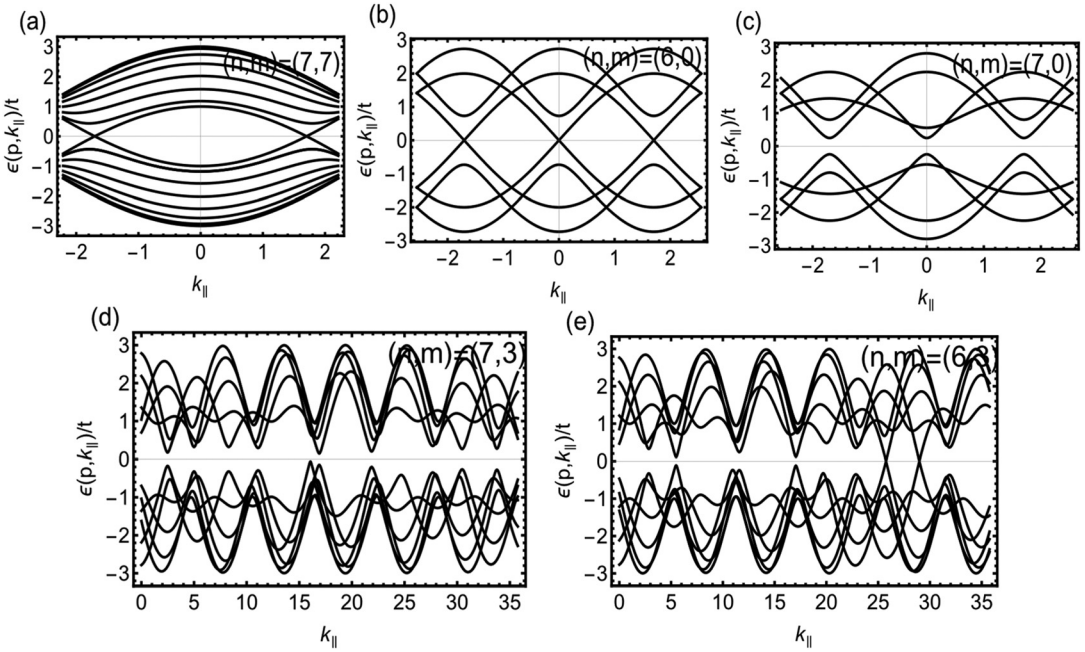


**Fig. 2** The band structure of carbon nanotubes. (a) Band structure of carbon armchair nanotubes ($n$,$m$) = (7,7), which is plotted using eqn (16). (a) and (c) Band structure of carbon zigzag nanotubes, where ($n$,$m$) = (6,0) for (b), which is a metal tube, and ($n$,$m$) = (7,0) for (c), which is a semiconductor tube; both graphs are plotted using eqn (17). (a) and (c) Band structures of carbon chiral nanotubes, where ($n$,$m$) = (7,3) in (b), which is a semiconductor tube (7 × 2 + 3 = 17 is not a multiple of 3), and ($n$,$m$) = (6,3) for (c), which is a metal tube (6 × 2 + 3 = 15 is a multiple of 3), (d) and (e), are plotted using eqn (15).

wavevector lines (cutting lines) intersect at the Dirac points. Consequently, armchair nanotubes exhibit no band gap and are thus classified as metallic. In contrast, zigzag and chiral nanotubes may either possess a band gap or not, depending on their chiral indices. Those exhibiting a band gap are classified as semiconductors, whereas those without a gap are considered metallic. This classification prompts the following question: What determines whether a nanotube is metallic or semiconducting?

The electronic behavior of a carbon nanotube with chiral indices ($n$,$m$) is governed by the positions of the cutting lines relative to the Dirac points in the Brillouin zone of graphene. If one or more cutting lines pass through a Dirac point, the conduction and valence bands touch, resulting in a zero-band gap and metallic behavior. Conversely, if none of the cutting lines intersect the Dirac points, the nanotube exhibits a band gap and behaves as a semiconductor. The variance between the metal and semiconductor tubes of zigzag and chiral tubes depends on the nanotube indices. Moreover, the Dirac points in a metal nanotube must be included in one (or more) of the allowed wave vector lines.[26,54] Hence, these facts could be used to derive an expression that helps to form the classification criterion. Fig. 3 shows the cutting lines on the graphene sheet for a semiconductor and a metal nanotube. In metal nanotubes, the projection of the vector that links the center of the graphene Brillouin zone is $\boldsymbol{XK}$, with the Dirac point $\boldsymbol{K_1}$ being $\boldsymbol{YK}$. This vector, $\boldsymbol{YK}$, must be an integer value of $\boldsymbol{K_1}$ if the allowed wave vectors (cutting lines) pass through Dirac

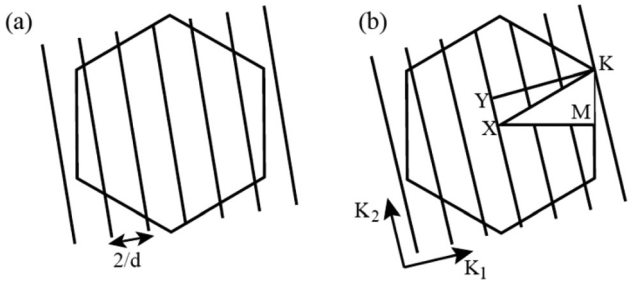


**Fig. 3** (a) Nanotube energy dispersion for semiconductor tubes, where none of the energy-crossing lines pass through Dirac points. (b) Energy dispersion of a metal tube where the energy-crossing line passes through Dirac points.

points. The projection of $\boldsymbol{XK}$ can be calculated from the vector geometry as:

$$\boldsymbol{XK} = \frac{|\boldsymbol{XK}\cdot\boldsymbol{K_1}|}{|\boldsymbol{K_1}|}, \boldsymbol{K_1} = \frac{2n+m}{3}\boldsymbol{K_1}. \quad (18)$$

$\boldsymbol{YK}$ has an integer value of $\boldsymbol{K_1}$ only if $2n + m$ (or $n - m$) is a multiple of 3, which means that the nanotube is a metal tube only if $2n + m$ is an integral multiple of 3.[26] Armchair nanotubes ($n = m$) satisfy this condition, and they are classified as metal tubes (see Fig. 2(a), where 6 × 2 = 12 is a multiple of 3). The zigzag nanotube is a metal only if $n$ is a multiple of 3 (Fig. 2(b)). The chiral tubes vary between the metal and

 

the semiconductor depending on the chiral indices (Fig. 2(d and e)).

The plotted graphs of the energy dispersion for the zigzag and chiral nanotubes show a distinct value of the energy at Dirac points K and K′. The difference between these distinct values of energy is known as the mismatch energy. This mismatch in energy is attributed to curvature-induced symmetry breaking and circumferential confinement. This energy can be estimated as the difference between the values of the valence energy bands at the Dirac points $\delta = |\varepsilon_i^+(\mathrm{K}) - \varepsilon_i^+(\mathrm{K}')|$. The magnitude of this energy is small compared with the quantized energies and the Coulomb energy, but it plays an important role in the stability of valley qubits by maintaining coherence for a long time, facilitating valley polarization and controlling valley currents in the valleytronic region.[54,55]

A simplified form of energy depression of carbon nanotubes can be derived if $k_x$ and $k_y$ are replaced by their values in terms of $k_\perp$ and $k_\parallel$.[45–60] The simplified form is $\varepsilon^\pm = \pm\hbar v_\mathrm{F}\sqrt{{k_\perp}^2 + {k_\parallel}^2}$. In this form, the circumference component $k_\perp$ could approach $k_\perp = K_\perp + \kappa_\perp$, where $k_\perp$ is the projection of $\boldsymbol{k}$ on $K_1$. The confinement along the tube circumference imposes discrete values of momentum, which means that $\boldsymbol{C_h}(k_\perp + \kappa_\perp) = 2\pi\upsilon$. The geometric calculation gives $\kappa_\perp = \frac{2}{\boldsymbol{d}}\left(\frac{n-m}{3} + \upsilon\right)$. In the case of a semiconductor tube, the Dirac points are missed, and $n - m = \pm 1$. Hence, the energy dispersion relation takes the following form:

$$\varepsilon^\pm = \pm\hbar v_\mathrm{F}\sqrt{\left(\frac{2}{\boldsymbol{d}}\right)^2\left(\upsilon \pm \frac{1}{3}\right)^2 + {k_\parallel}^2}. \tag{19}$$

The energy gap of semiconductor nanotubes is related to the chiral indices and can be calculated by $\varepsilon_\mathrm{g} = \varepsilon^+(k_\parallel = 0) - \varepsilon^-(k_\parallel = 0)$. If the last derived equation is used, the energy gap will be $\varepsilon_\mathrm{g} = 4\hbar v_\mathrm{F}/3d = 0.72/d(nm)$ eV.

### 2.3. Carbon nanotube quantum dots

In the case of a finite length "$L$" nanotube with $M$ unit cells ($M = L/|T|$), the electrons would also be confined along the tube axis. This would make this tube a 0D material (quantum dot), wherein the allowed values of momentum $k_\parallel$, in this case, would be converted from continuous values to quantized values. The allowed values of $k_\parallel$ would be

$$M\boldsymbol{k}_\parallel\boldsymbol{T} = p2\pi \Rightarrow \boldsymbol{k}_\parallel = p\frac{2\pi}{M|\boldsymbol{T}|} = p\frac{\pi}{L};\quad p = 1, 2, \ldots (N_\mathrm{C} - 1). \tag{20a}$$

This condition imposes that the tube ends with hard-wall boundaries. In general, the tube could end with different boundaries (suppose right R and left L boundaries). The shape of the tube boundary adds a phase shift to the quantization condition. The modified condition is:[61]

$$k_\parallel = k_\parallel = \frac{\pi l_\mathrm{p}}{N_\mathrm{s} + 1} - \frac{2\theta_r}{N_\mathrm{s} + 1} \tag{20b}$$

with

$$\theta_r = \pm\frac{1}{2}\varphi_r + (2m + 1)\frac{\pi}{2}$$

where $N_\mathrm{s}$ is the number of graphene unit cells along the nanotube axis, $r = \pm 1$ represents the branch index ($r = 1$ right-going branch and $r = -1$ left branch), $p$ is the parity index ($r = 1$ for even parity with a symmetric wavefunction, while $r = -1$ for odd parity with an antisymmetric wavefunction), $\theta_r$ is the phase shift of the branch which could be determined by the boundary condition, and $\varphi_r = \arg(S(k))$, where $S(k) = \sum_j^3 t e^{ik\Delta l_j}$ is the graphene tight-binding structure factor.[61] In the next discussion, we will consider the first form of the quantization condition. The quantization energy of the carbon nanotube quantum dot (CNTQD) levels can be obtained from eqn (16) after replacing the continuous $\boldsymbol{k}_\parallel$ with the corresponding quantized values derived from the preceding equations. A simplified form of the CNTQD energy level would result from eqn (19) after considering quantized $\boldsymbol{k}_\parallel$,[45,60] which leads to

$$\varepsilon_\mathrm{p} = \sqrt{\frac{{\varepsilon_\mathrm{g}}^2}{4} + \left(\hbar v_\mathrm{F}\frac{p\pi}{L}\right)^2}. \tag{21}$$

Every quantized level can be occupied by two electrons with different spin directions. However, graphene shows two inequivalent valleys at the Dirac points because of the time-reversal symmetry. The electrons could be in either the K valley or the K′ valley, which means that these valleys add a second degree of freedom. In other words, every quantum level consists of two sublevels at the K and K′ valleys (valley sublevels), and every valley sublevel can be occupied by two electrons owing to spin degeneracy. This results in a total of four electrons that can occupy each quantum level.[54–56,58–61] These electrons interact with each other *via* Coulomb interactions. If the constant interaction model (CIM) is used to describe the CNTQDs, the chemical potential of the CNTQDs can be determined as follows:

$$\begin{aligned} E_{\mathrm{p},l} = {} & \sqrt{\frac{{\varepsilon_\mathrm{g}}^2}{4} + \left(\hbar v_\mathrm{F}\frac{p\pi}{L}\right)^2} + [4(p-1) + l]U_\mathrm{c} \\ & + [p\delta_{l,2} - (p-1)\delta_{l,0}]\delta. \end{aligned} \tag{22}$$

where $l = 0$, 1, 2, and 3 ensures the inclusion of the valley and spin degeneracy of every level $p$. $U_\mathrm{c}$ is the Coulomb energy unit $U = e^2/C_\Sigma$ (where $C_\Sigma = 2\pi\varepsilon_0 L/\ln(b/a)$ is the total capacitance of the CNTQD when the tube is considered a cylindrical capacitor; $L$ is the tube length). The valley sublevel mismatch $\delta$ has been added, where $\delta_{l,2}$ is a Kronecker delta function that ensures that $\delta$ is added after every valley sublevel is filled. A scheme of the energy level of a CNTQD with its sublevels is shown in Fig. 4, where the four sublevels differ.[55] The energy required to add an electron to every sublevel is given by

$$\begin{aligned} \Delta E_{\mathrm{p},1} &= E_\mathrm{add} = E_\mathrm{c} \\ \Delta E_{\mathrm{p},2} &= E_\mathrm{add} = E_\mathrm{c} + \delta \\ \Delta E_{\mathrm{p},3} &= E_\mathrm{add} = E_\mathrm{c} \\ \Delta E_{\mathrm{p},4} &= E_\mathrm{add} = \Delta\varepsilon - \delta + E_\mathrm{c} \end{aligned} \tag{23}$$

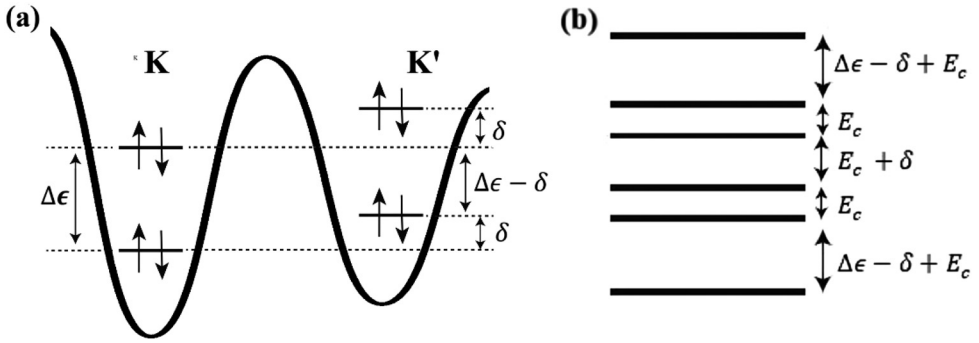


**Fig. 4** Energy levels of the CNTQDs. (a) Scheme illustrating the CNT valleys and how to generate a new degree of freedom in CNTQDs with mismatch energy. (b) Energy levels of the CNTQDs and the additional charge energy required to enable an electron to occupy every level.



where $E_{\mathrm{add}}$ is the addition energy, $\Delta\varepsilon = E_{\mathrm{p}+1,l} - E_{\mathrm{p},l}$ is the separation between the quantized levels, and $E_{\mathrm{c}}$ is the charge energy, which is equal to the Coulomb energy unit $U_{\mathrm{c}}$.

## 3. Blockade phenomena and stability diagram

The single electron transistor based on CNTQDs consists of a CNTQD that is coupled to conducting electrodes from the left and right, which form the source and drain. A voltage ($V$) must be applied to the electrodes to create a difference in their chemical potential, which is known as a bias window. The difference in chemical potential forces electrons to flow from a higher electrode chemical potential (which acts as a source) to a lower electrode chemical potential (which acts as a drain). However, electrons can flow only if one (or more) energy level is located within the bias window. The energy of the dot level can be replaced or modified by applying another voltage through a third electrode that must be connected to the CNTQD, which is called the gate electrode with voltage $V_{\mathrm{g}}$. Moreover, single-electron transport phenomena can be observed if the thermal energy $kT$ is smaller than the separation between energy levels in the QDs.[58–63] The variations in the thermal energy, quantum energy levels, and Coulomb interaction lead to a difference between the two systems. The first is when the thermal energy is greater than the quantum energy and less than the Coulomb energy. This regime is classified as a metallic Coulomb blockade regime. The second is where the thermal energy is smaller than both the Coulomb energy and the quantum energy. This regime is known as the quantum Coulomb blockade regime. In CNT QDs, the energy of the quantum level is greater than the thermal energy, and the SET based on CNT QDs can be categorized into a quantum Coulomb blockade regime. In the quantum-Coulomb blockade regime, an electron can be transported through a QD if it has sufficient energy to occupy the quantum energy level and overcome the Coulomb repulsive interaction. This sufficient energy can be provided to electrons by applied voltages. In the constant energy model, the QD is considered a capacitor, and the Coulomb energy is treated as the charging energy of this capacitor. We have three electrodes in the SET: the source, drain, and gate. The total capacity $C_{\Sigma}$ is divided by the capacity of the source $C_{\mathrm{s}}$, the capacity of the drain $C_{\mathrm{d}}$, and the capacity of the gate $C_{\mathrm{g}}$ ($C_{\Sigma} = C_{\mathrm{d}} + C_{\mathrm{s}} + C_{\mathrm{g}}$). The capacities of these capacitors $C_{\mathrm{s}}$, $C_{\mathrm{d}}$, and $C_{\mathrm{g}}$, depend on the spatial arrangement of the electrodes relative to the QD. These capacities could also be defined from the experimental data of any Coulomb diamond by defining the intersection points.

Electron transport from the source (or drain) to (from) the QD that has $N$ electrons when the source (or drain) chemical potential aligns with the QD level $E_{\mathrm{p},l}$. This statement leads us to write:[63]

$$V = \frac{2}{e[1+\zeta]}\left[E_{\mathrm{p},l} + E_{\mathrm{add}} - e\frac{V_{\mathrm{g}}C_{\mathrm{g}}}{C_{\Sigma}}\right] \tag{24}$$

$$V = \frac{2}{e[1+\zeta]}\left[E_{\mathrm{p},l} - e\frac{V_{\mathrm{g}}C_{\mathrm{g}}}{C_{\Sigma}}\right] \tag{25}$$

$$V = \frac{2}{e[\zeta-1]}\left[E_{\mathrm{p},l} - e\frac{V_{\mathrm{g}}C_{\mathrm{g}}}{C_{\Sigma}}\right] \tag{26}$$

$$V = \frac{2}{e[\zeta-1]}\left[E_{\mathrm{p},l} + E_{\mathrm{add}} - e\frac{V_{\mathrm{g}}C_{\mathrm{g}}}{C_{\Sigma}}\right] \tag{27}$$

where $\zeta = \dfrac{C_{\mathrm{d}} - C_{\mathrm{s}}}{C_{\Sigma}}$ is an asymmetric parameter and where $C_{\Sigma}$ is the total capacity of the CNTQDs. These equations represent four straight equations that intersect with each other and define the borders between the values of the applied voltage, which can provide electrons with the energy required for transport, and those that cannot. Moreover, from the intersection points of these lines, the operation conditions of the CNTQD devices could be extracted. The intersection points are:[63]

 

$$\begin{aligned} A(V_g[A], V[A]) &= \left(\frac{E_{p,l}C_\Sigma}{eC_g} + \frac{1}{e}\frac{C_g + 2C_s}{2C_g}E_{add},\ \frac{1}{e}E_{add}\right) \\ B(V_g[B], V[B]) &= \left(\frac{C_\Sigma}{eC_g}[E_{p,l} + E_{add}],\ 0\right) \\ C(V_g[C], V[C]) &= \left(\frac{E_{p,l}C_\Sigma}{eC_g} + \frac{1}{e}\frac{C_g + 2C_d}{2C_g}E_{add},\ -\frac{1}{e}E_{add}\right) \\ D(V_g[D], V[D]) &= \left(\frac{C_\Sigma}{eC_g}E_{p,l},\ 0\right) \end{aligned} \tag{28}$$

From these points, the maximum source–drain voltage that can be applied, the positions of conductance peaks, and the voltage range where Coulomb blockade would be observed at zero value of source–drain voltage could be given by:[62]

$$V = \frac{1}{e}E_{add} \tag{29}$$

$$V_g = \frac{C_\Sigma}{eC_g}[E_{p,l} + E_{add}] \tag{30}$$

$$\Delta V_g = \frac{C_\Sigma}{eC_g}E_{add} \tag{31}$$

Using eqn (24)–(27), the stability diagram of the CNTQDs can be plotted for any dot. Fig. 5(a) shows the stability diagram of metallic CNTQDs (where $\varepsilon_g = 0$) which has $E_c$ = 4.5 meV and $\Delta E$ = 6.8 ± 2.5 meV (data are taken from ref. 64). The gray diamonds in Fig. 5(a) represent the diamonds of the quantum-Coulomb blockade, where the applied voltages cannot provide electrons for transport through the CNTQDs.

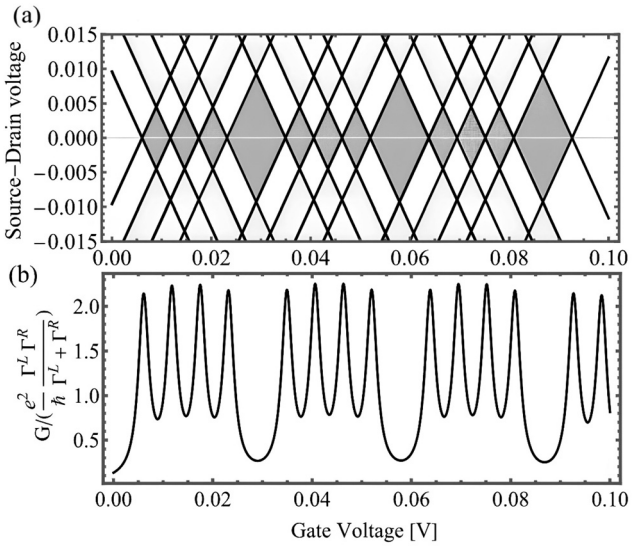


**Fig. 5** Stability diagram and the conductance of metallic CNTQDs. (a) Stability diagram of CNTQDs, plotted by using eqn (24)–(27). The CNTQDs used in this study are fabricated from a metallic tube (*i.e.*, $\varepsilon_g$ = 0 and the mismatch energy is assumed to be $\delta$ = 0; the tube is connected to the source and drain *i.e.*, $\zeta$ = 0 also) and it has $E_c = 4.5 \times 10^{-3}$ eV and $\Delta E$ = 6.8 ± 2.5 meV (data taken from ref. 64). (b) Conductance of the tunneling resonance system based on CNTQDs, which is plotted using eqn (42), where the tunneling rates are assumed to be $\Gamma^{L/R} = 1 \times 10^{-3}$ eV.

The other diamonds represent the values of the applied voltages that enable electron transport. As shown, the quantum-Coulomb diamond size depends on the CNTQD level. The size of the diamonds depends on the quantum dot chirality indices. For smaller quantum dots (QDs) with reduced $n$ and $m$ values, the Coulomb diamond is larger, requiring higher voltages to control CNTQD devices. This results in improved controllability and reduced sensitivity to environmental fluctuations. By leveraging the stability diagram, these devices can be designed for applications such as single-electron transistors, spin qubits, or charge qubits, depending on operational requirements.

Finally, it should be noted that altering the configuration of the connected electrodes leads to corresponding changes in the capacitances $C_s$, $C_d$, and $C_g$. Consequently, the stability diagram of CNTQDs is affected, as the range of applied voltages in which the Coulomb blockade effect is observed and the range where it is not both vary accordingly. As evident from eqn (29), the maximum source–drain voltage is independent of the system capacitances; therefore, modifying the electrode configuration does not influence the source–drain voltage range, which depends solely on the quantum dot size. Eqn (31) shows that the range of gate voltage over which the blockade effect occurs is proportional to $C_\Sigma/eC_g$. Hence, decreasing the gate capacitance extends this range. Such an extended gate-voltage range enables more precise control over the occupation of quantum dot energy levels during the operation of CNTDQ-based devices. Furthermore, the capacitances of the source, drain, and gate electrodes can be extracted from the experimental data by identifying the intersection points of any Coulomb diamonds in the stability diagram. These intersection coordinates can then be substituted into the corresponding equations (eqn (28)) to form a solvable set, allowing the determination of $C_s$, $C_d$, and $C_g$.

## 4. Conductance in CNTQDs

Electron transport over short distances in nanodevices preserves the quantum information encoded in the electron's wavefunction phase factor, a process known as quantum transport. Moreover, the transport phenomenon itself occurs when a physical system transitions from equilibrium to nonequilibrium conditions, such as when a bias voltage is applied. To study electron transport in quantum devices while accounting for its quantum nature, the Keldysh formalism for nonequilibrium systems is commonly employed. In CNTQDs, electron transport under applied voltages is treated as quantum transport, and this formalism is used to analyze electrical conductance.

We consider the Anderson model, where a QD is coupled symmetrically to noninteracting electrodes. The corresponding Hamiltonian of this system can be written as.[65–67]

$$H = \sum_\alpha H_\alpha + H_T + H_D \tag{32}$$

with,

$$H_\alpha = \sum_{k\sigma\alpha} \varepsilon_{ak\sigma} c^\dagger_{\alpha k\sigma} c_{\alpha k\sigma}; \quad \alpha = \mathrm{L}, \mathrm{R} \tag{33}$$

$$H_\mathrm{T} = \sum_{k\sigma\alpha}\sum_{n} [V_{\alpha k\sigma,n\sigma} c^\dagger_{\alpha k\sigma} d_{n\sigma} + h\cdot c] \tag{34}$$

$$H_\mathrm{QD} = H_\mathrm{D} + H_{\mathrm{D(e-e)}} = \sum_n \varepsilon_{n\sigma} d^\dagger_{n\sigma} d_{n\sigma} + \frac{1}{2}\sum_{nn'} U_{nn'} d^\dagger_{n\sigma} d^\dagger_{n'\sigma} d_{n'\sigma} d_{n\sigma} \tag{35}$$

where $H_\alpha$; $\alpha$ = L, R are the electrode Hamiltonians, $H_\mathrm{T}$ is the tunnelling Hamiltonian, and $H_\mathrm{D}$ is the CNTQD Hamiltonian. Here, $c_{\alpha k\sigma}$ ($c^\dagger_{\alpha k\sigma}$) destroys (creates) a conduction electron with momentum $\boldsymbol{k}$ and spins $\sigma$ at electrode $\alpha$, and $d_{n\sigma}$ ($d^\dagger_{n\sigma}$) destroys (creates) an electron with spin $\sigma$ in the QD. where $\varepsilon_{\alpha k\sigma}$ is the kinetic energy of electrons in the electrode, $V_{k\sigma\alpha,n\sigma}$ ($V^*_{k\sigma\alpha,n\sigma}$) represents the matrix elements of the tunnelled electrons, $\varepsilon_{d\sigma}$ is the energy dot level, and $U_{nn'}$ is the interaction potential.[67–72] In the constant interaction model where the electrons are assumed to interact with the same energy ($U_{nn'} = U$), the electron–electron interaction Hamiltonian is:[55,59]

$$H_{\mathrm{D(e-e)}} \approx \frac{U}{2}\left[\left(\sum_n d^\dagger_{n\sigma} d_{n\sigma}\right)^2 - \sum_n \left(d^\dagger_{n\sigma} d_{n\sigma}\right)^2\right] = U\frac{N(N-1)}{2} \tag{36}$$

where $(d^\dagger_{n\sigma} d_{n\sigma})^2 = {n_{n\sigma}}^2 = n_{n\sigma} = 1$, the number of electrons in the CNTQD is $\sum_n n_{n\sigma} = N$, and $U = e^2/C_\Sigma$. The Coulomb interaction can be added to the dot-level energy as $\bar{\varepsilon}_{n\sigma} = \varepsilon_{n\sigma} + UN(N-1)/2$. The linear conductance through the CNTQD can be given by the Landauer–Büttiker formula:[66–69]

$$G = \frac{e^2}{\hbar}\sum_{\alpha=\mathrm{L,R}} \int_{\mu_\mathrm{R}}^{\mu_\mathrm{L}} \left(-\frac{\partial f_\alpha(\varepsilon)}{\partial\varepsilon}\right) \mathbf{Tr}\left[\frac{\Gamma^\mathrm{L}(\varepsilon)\Gamma^\mathrm{R}(\varepsilon)}{\Gamma^\mathrm{L}(\varepsilon)+\Gamma^\mathrm{R}(\varepsilon)} A(\varepsilon)\right] \tag{37}$$

where $f_\alpha(\varepsilon)$ is the Fermi distribution function, $\Gamma^\mathrm{L}(\varepsilon)(\Gamma^\mathrm{R}(\varepsilon))$ is the tunneling rate from the left (right) electrode, which behaves as a source (drain), and $A(\varepsilon)$ is a spectral function that has the following form:

$$A(\varepsilon) = \frac{1}{\pi}\frac{\Im\mathrm{m}\Sigma^\mathrm{R}(\varepsilon)}{[\varepsilon - \varepsilon_\mathrm{d} - \Re\mathrm{e}\Sigma^\mathrm{R}(\varepsilon)]^2 + [\Im\mathrm{m}\Sigma^\mathrm{R}(\varepsilon) + \eta]^2} \tag{38}$$

where $\Re\mathrm{e}\Sigma^\mathrm{R}(\varepsilon)$ ($\Im\mathrm{m}\Sigma^\mathrm{R}(\varepsilon)$) is the real part (imaginary part) of self-energies, which must be defined. The self-energies can be extracted from the equilibrium self-energies of the causal Green function (GF) after applying the Langreth rules. The causal Green's function is obtained by modeling the tunneling Hamiltonian as perturbed, with the dot Hamiltonian acting as the unperturbed foundation. This leads to

$$G_{nm\sigma}(t,t') = -i\left\langle \hat{T} \mathrm{e}^{-\frac{i}{\hbar}\int H_\mathrm{T}(\mathbf{1})_\mathrm{I}\mathrm{d}1} d_{n\sigma}(t) d^\dagger_{m\sigma}(t')\right\rangle \tag{39}$$

Considering the first-order corrections and then applying Wick's theory, one could gate the tunneling self-energy $\Sigma_\mathrm{T} = \frac{1}{\hbar}\sum_{ak\sigma} V_{k\sigma\alpha,l} V^*_{k\sigma\alpha,p} g_{k\sigma\alpha}(t_1,t_2)$. The next steps involve applying Langreth's rules and conducting a Fourier transformation into energy space, which yields the following tunnelling self-energy expressions for each dot level "$l$".

$$\Sigma^{-+}_{\mathrm{T},ll}(\varepsilon) = \frac{i}{\hbar}\sum_\alpha f_\alpha(\varepsilon)\Gamma^\alpha_{ll}(\varepsilon) \tag{40}$$

$$\Sigma^{\mathrm{R/A}}_{\mathrm{T},ll}(\varepsilon) = \Lambda_{lp}(\varepsilon) \mp \frac{i}{2}\sum_\alpha \Gamma^\alpha_{ll}(\varepsilon) \tag{41}$$

where $\sum^{-+}_\mathrm{T}$ and $\sum^{\mathrm{R/A}}_\mathrm{T}$ are the lesser, retarded, and advanced tunnelling self-energies, respectively. Under the wide-band approximation, the real part could be neglected compared with other energies, and the tunnelling rate's imaginary part "$\Gamma_{li(\varepsilon)}$" could be approximated to its value at the Fermi level of electrodes and considered constant for all dot levels ($\Gamma^\alpha_{ll}(\varepsilon) = \Gamma^\alpha$). Hence, after the self-energies in the spectral function are substituted, the conductance expression is as follows: one can find the following expressions for conductance:

$$G = \frac{e^2}{\pi\hbar}\frac{\Gamma^\mathrm{L}\Gamma^\mathrm{R}}{\Gamma^\mathrm{L}+\Gamma^\mathrm{R}}\sum_n\sum_{\alpha=\mathrm{L,R}}\left[\frac{\sum_\alpha \Gamma^\alpha/2}{[\mu_\alpha - \bar{\varepsilon}_n]^2 + [\sum_\alpha \Gamma^\alpha/2]^2}\right] \tag{42}$$

The plot of the derived expression of conductance is shown in Fig. 5(b), where eqn (42) is plotted for $V = 0$. The CNTQDs present peaks of conductance, which means that the conductivity of the CNTQDs is quantified. Starting from the ground state, when an electron passes through a CNTQD, the energy required to occupy the ground state at the lowest energy during pass is $\varepsilon_1$. Hence, the first peak would be obtained. With increasing gate voltage, electrons can pass through the second sublevel, and the second peak will appear at $V_\mathrm{g} = C_\Sigma[\varepsilon_1 + U]/eC_\mathrm{g}$. The third peak will appear because of the first level of the second valley, where this peak would appear at $V_\mathrm{g} = C_\Sigma[\varepsilon_1 + 2U]/eC_\mathrm{g}$. The fourth peak is obtained when an electron passes through the second valley sublevel in the second valley, and this peak appears at $V_\mathrm{g} = C_\Sigma[\varepsilon_1 + 3U]/eC_\mathrm{g}$. The same discussion could be held for higher quantized levels and their spins and valley sublevels. As a result, the conductance peaks in the CNTQD group into sets of four peaks, which has been reported in many works.

## 5. Conclusion

This study provides a detailed theoretical framework for understanding the electronic properties of carbon nanotube quantum dots (CNTQDs). By employing the constant interaction model (CIM) and Green's function formalism, we derived the quantized energy levels of CNTQDs and analyzed their stability diagrams under Coulomb blockade regimes. This study illustrates that spin and valley degeneracies lead to four distinct conductance peaks per quantized energy level, a key feature of quantum transport in CNTQDs. Furthermore, we investigated how the chiral indices ($n$,$m$) affect the type of carbon nanotube and energy levels of CNTQDs, which could

 

be considered as design parameters when carbon nanotube-based devices are fabricated. Stability diagrams revealing diamond-shaped blockade regions offer insights into the control of single-electron tunneling in CNTQD-based devices. These overview studies provide researchers with the necessary information about the electronic structures of CNTs and CNTQDs, which will help in designing and controlling CNT-based devices.

## Conflicts of interest

There are no conflicts to declare.

## Data availability

All data supporting the findings of this study are included within the main article. No additional datasets were generated or analyzed.



## References

1 H. N. Khan, D. A. Hounshell and E. R. H. Fuchs, *Nat. Electron.*, 2018, **1**, 14–21.
2 M. Schulz, *Nature*, 1999, **399**, 729–730.
3 D. Mamaluy and X. Gao, *Appl. Phys. Lett.*, 2015, **106**, 193503.
4 V. V. Zhirnov, R. K. Cavin, J. A. Hutchby and G. I. Bourianoff, *Proc. IEEE*, 2003, **91**, 1934–1939.
5 S. Lee, Y. Lee, E. B. Song and T. Hiramoto, *Nano Lett.*, 2013, **14**, 71–77.
6 A. Lubow, S. Ismail-Beigi and T. P. Ma, *Appl. Phys. Lett.*, 2010, **96**, DOI: 10.1063/1.3367708.
7 Y. Zhang, L. F. Duan, Y. Zhang, J. Wang, H. Geng and Q. Zhang, *Nano-Micro Lett.*, 2013, **6**, 1–19.
8 D. Kim, Z. Shi, C. B. Simmons, D. R. Ward, J. R. Prance, T. S. Koh, J. K. Gamble, D. E. Savage, M. G. Lagally, M. Friesen, S. N. Coppersmith and M. A. Eriksson, *Nature*, 2014, **511**, 70–74.
9 R. J. Warburton, *Nat. Mater.*, 2013, **12**, 483–493.
10 N. W. Hendrickx, W. I. L. Lawrie, M. Russ, F. van Riggelen, S. L. de Snoo, R. N. Schouten, A. Sammak, G. Scappucci and M. Veldhorst, *Nature*, 2021, **591**, 580–585.
11 C. H. Yang, R. C. C. Leon, J. C. C. Hwang, A. Saraiva, T. Tanttu, W. Huang, J. Camirand Lemyre, K. W. Chan, K. Y. Tan, F. E. Hudson, K. M. Itoh, A. Morello, M. Pioro-Ladrière, A. Laucht and A. S. Dzurak, *Nature*, 2020, **580**, 350–354.
12 A. Javey, J. Guo, Q. Wang, M. Lundstrom and H. Dai, *Nature*, 2003, **424**, 654–657.
13 Z. Chen, J. Appenzeller, J. Knoch, Y. M. Lin and P. Avouris, *Nano Lett.*, 2005, **5**, 1497–1502.
14 K. Natori, Y. Kimura and T. Shimizu, *J. Appl. Phys.*, 2005, **97**, DOI: 10.1063/1.1840096.
15 S. J. Wind, J. Appenzeller and P. Avouris, *Phys. Rev. Lett.*, 2003, **91**, 058301.
16 M. D. Bishop, G. Hills, T. Srimani, C. Lau, D. Murphy, S. Fuller, J. Humes, A. Ratkovich, M. Nelson and M. M. Shulaker, *Nat. Electron.*, 2020, **3**, 492–501.
17 G. Hills, C. Lau, A. Wright, S. Fuller, M. D. Bishop, T. Srimani, P. Kanhaiya, R. Ho, A. Amer, Y. Stein, D. Murphy, Arvind, A. Chandrakasan and M. M. Shulaker, *Nature*, 2019, **572**, 595–602.
18 E. A. Laird, F. Pei and L. P. Kouwenhoven, *Nat. Nanotechnol.*, 2013, **8**, 565–568.
19 J. S. Chen, K. J. Trerayapiwat, L. Sun, M. D. Krzyaniak, M. R. Wasielewski, T. Rajh, S. Sharifzadeh and X. Ma, *Nat. Commun.*, 2023, **14**, 848.
20 C. Galland and A. Imamoğlu, *Phys. Rev. Lett.*, 2008, **101**, 157404.
21 I. Khivrich and S. Ilani, *Nat. Commun.*, 2020, **11**, 2299.
22 Z. V. Penfold-Fitch, F. Sfigakis and M. R. Buitelaar, *Phys. Rev. Appl.*, 2017, **7**, 054017.
23 F. Pei, E. A. Laird, G. A. Steele and L. P. Kouwenhoven, *Nat. Nanotechnol.*, 2012, **7**, 630–634.
24 L. Huang, G. Wei and A. R. Champagne, *Phys. Rev. Appl.*, 2025, **23**, 014030.
25 H. Wang and G. Burkard, *Phys. Rev. B: Condens. Matter Mater. Phys.*, 2015, **92**, 195432.
26 J. C. Charlier, X. Blase and S. Roche, *Rev. Mod. Phys.*, 2007, **79**, 677.
27 J. W. Mintmire and C. T. White, *Carbon*, 1995, **33**, 893–902.
28 Y. Q. Feng, R. Q. Zhang, K. S. Chan, H. F. Cheung and S. T. Lee, *Phys. Rev. B: Condens. Matter Mater. Phys.*, 2002, **66**, 045404.
29 J. Haruyama, I. Takesue, T. Hasegawa and Y. Sato, *Phys. Rev. B: Condens. Matter Mater. Phys.*, 2001, **63**, 073406.
30 S. J. Sque, R. Jones, S. Öberg and P. R. Briddon, *Phys. Rev. B: Condens. Matter Mater. Phys.*, 2007, **75**, 115328.
31 J. Feng, K. Liu, M. Graf, D. Dumcenco, A. Kis, M. Di Ventra and A. Radenovic, *Nat. Mater.*, 2016, **15**, 850–855.
32 J. Wu, K. Gerstandt, H. Zhang, J. Liu and B. J. Hinds, *Nat. Nanotechnol.*, 2012, **7**, 133–139.
33 W. Izumida, R. Okuyama, A. Yamakage and R. Saito, *Phys. Rev. B*, 2016, **93**, 195442.
34 A. Pályi and G. Burkard, *Phys. Rev. B: Condens. Matter Mater. Phys.*, 2010, **82**, 155424.
35 A. Bhaumik, S. Nori, R. Sachan, S. Gupta, D. Kumar, A. K. Majumdar and J. Narayan, *ACS Appl. Nano Mater.*, 2018, **1**, 807–819.
36 J. S. Jeong and H. W. Lee, *Phys. Rev. B: Condens. Matter Mater. Phys.*, 2009, **80**, 075409.
37 C. S. Peça, L. Balents and K. J. Wiese, *Phys. Rev. B: Condens. Matter Mater. Phys.*, 2003, **68**, 205423.
38 W. Liang, M. Bockrath, D. Bozovic, J. H. Hafner, M. Tinkham and H. Park, *Nature*, 2001, **411**, 665–669.
39 M. Bockrath, D. H. Cobden, P. L. McEuen, N. G. Chopra, A. Zettl, A. Thess and R. E. Smalley, *Science*, 1997, **275**, 1922–1925.
40 H. W. C. Postma, T. Teepen, Z. Yao, M. Grifoni and C. Dekker, *Science*, 2001, **293**, 76–79.

41 Z. K. Tang, L. Zhang, N. Wang, X. X. Zhang, G. H. Wen, G. D. Li, J. N. Wang, C. T. Chan and P. Sheng, *Science*, 2001, **292**, 2462–2465.
42 J. González, *Phys. Rev. Lett.*, 2002, **88**, 076403.
43 N. Murata, J. Haruyama, J. Reppert, A. M. Rao, T. Koretsune, S. Saito, M. Matsudaira and Y. Yagi, *Phys. Rev. Lett.*, 2008, **101**, 027002.
44 Y. Liu, Y. Shen, L. Sun, J. Li, C. Liu, W. Ren, F. Li, L. Gao, J. Chen, F. Liu, Y. Sun, N. Tang, H. M. Cheng and Y. Du, *Nat. Commun.*, 2016, **7**, 10921.
45 O. Lesser, G. Shavit and Y. Oreg, *Phys. Rev. Res.*, 2020, **2**, 023254.
46 W. Izumida, L. Milz, M. Marganska and M. Grifoni, *Phys. Rev. B*, 2017, **96**, 125414.
47 J. P. Cleuziou, W. Wernsdorfer, V. Bouchiat, T. Ondarcuhu and M. Monthioux, *Nat. Nanotechnol.*, 2006, **1**, 53–59.
48 X. Ma, N. F. Hartmann, J. K. S. Baldwin, S. K. Doorn and H. Htoon, *Nat. Nanotechnol.*, 2015, **10**, 671–675.
49 T. Mueller, M. Kinoshita, M. Steiner, V. Perebeinos, A. A. Bol, D. B. Farmer and P. Avouris, *Nat. Nanotechnol.*, 2009, **5**, 27–31.
50 E. Kymakis and G. A. J. Amaratunga, *Appl. Phys. Lett.*, 2002, **80**, 112–114.
51 T. A. Shastry and M. C. Hersam, *Adv. Energy Mater.*, 2017, **7**, 1601205.
52 S. Blien, P. Steger, N. Hüttner, R. Graaf and A. K. Hüttel, *Nat. Commun.*, 2020, **11**, 1636.
53 L. Husel, J. Trapp, J. Scherzer, X. Wu, P. Wang, J. Fortner, M. Nutz, T. Hümmer, B. Polovnikov, M. Förg, D. Hunger, Y. H. Wang and A. Högele, *Nat. Commun.*, 2024, **15**, 3989.
54 S. V. Morozov, K. S. Novoselov and A. K. Geim, *Phys.-Usp.*, 2008, **51**, 727–748.
55 A. Moulhim, B. Tripathi and M. Kumar, *Phys. Scr.*, 2021, **96**, 125802.
56 S. Sapmaz, P. Jarillo-Herrero, L. P. Kouwenhoven and H. S. J. Van Der Zant, *Semicond. Sci. Technol.*, 2006, **21**, S52.
57 S. Das Sarma, S. Adam, E. H. Hwang and E. Rossi, *Rev. Mod. Phys.*, 2011, **83**, 407.
58 A. Moulhim, B. Tripathi and M. Kumar, *Micro Nanostruct.*, 2022, **168**, 207284.
59 D. Ryndyk, *Theory of quantum transport at nanoscale*, Springer Series in Solid-State Sciences, vol. 184, p. 9, DOI: 10.1007/978-3-319-24088-6.
60 E. A. Laird, F. Kuemmeth, G. A. Steele, K. Grove-Rasmussen, J. Nygård, K. Flensberg and L. P. Kouwenhoven, *Rev. Mod. Phys.*, 2015, **87**, 703.
61 W. Izumida, R. Okuyama and R. Saito, *Phys. Rev. B: Condens. Matter Mater. Phys.*, 2015, **91**, 235442.
62 J. Cao, Q. Wang and H. Dai, *Nat. Mater.*, 2005, **4**, 745–749.
63 A. Moulhim, B. Tripathi and M. Kumar, *Solid State Commun.*, 2020, **322**, 114078.
64 R. Leturcq, C. Stampfer, K. Inderbitzin, L. Durrer, C. Hierold, E. Mariani, M. G. Schultz, F. Von Oppen and K. Ensslin, *Nat. Phys.*, 2009, **5**, 327–331.
65 Y. Meir and N. S. Wingreen, *Phys. Rev. Lett.*, 1992, **68**, 2512.
66 A. P. Jauho, N. S. Wingreen and Y. Meir, *Phys. Rev. B: Condens. Matter Mater. Phys.*, 1994, **50**, 5528.
67 A. P. Jauho, N. S. Wingreen and Y. Meir, *Semicond. Sci. Technol.*, 1994, **9**, 926.
68 Y. Meir, N. S. Wingreen and P. A. Lee, *Phys. Rev. Lett.*, 1993, **70**, 2601.
69 L. Craco and K. Kang, *Phys. Rev. B: Condens. Matter Mater. Phys.*, 1999, **59**, 12244.
70 D. E. Liu and H. U. Baranger, *Phys. Rev. B: Condens. Matter Mater. Phys.*, 2011, **84**, 201308.
71 X. Li, H. Chen and S. X. Zhou, *Phys. Rev. B: Condens. Matter Mater. Phys.*, 1995, **52**, 12202.
72 D. Gerace, E. Pavarini and L. C. Andreani, *Phys. Rev. B: Condens. Matter Mater. Phys.*, 2002, **65**, 155331.